COB-2023-0506

AERODYNAMIC PERFORMANCE OF SG6043 PROFILE MODIFIED WITH BIOMIMETIC FOR SMALL WIND TURBINES APPLICATION

Luana Taís Puhl Schneider
Giuliano Demarco
Universidade Federal de Santa Maria, Programa de Pós Graduação em Engenharia Mecânica, Santa Maria
luana.schneider@acad.ufsm.br
giuliano.demarco@ufsm.br
Carlos Eduardo de Souza
Universidade Federal de Santa Maria, Curso de Engenharia Mecânica, campus Cachoeira do Sul
carlos.souza@ufsm.br

Abstract. *Replacing fossil fuels energy sources for renewable ones has been a goal with increasing interest in many countries, as well as the concern about environmental impacts caused by human activities. Despite the importance of expanding the installed capacity of wind turbines, it poses challenges for small wind turbines operating at low Reynolds numbers, resulting in reduced efficiency. Additionally, the smaller rotor diameter further impacts the performance of these turbines. Moreover, small wind turbines are limited by available technology and rely on high angles of attack to generate sufficient torque for overcoming resistance and initiating blade rotation. Thus, these preliminary study investigates the aerodynamic performance of the SG6043 airfoil profile, usually employed on small wind turbines, with and without biomimetic modifications. Inspired by the humpback whale's flipper, two three-dimensional airfoil models were developed, one with tubercles (bumps) on the leading edge and one without. The humpback whale, despite its massive size, exhibits remarkable maneuverability and improved performance due to the presence of leading-edge protuberances in its flippers. Using the OpenFOAM software, simulations were conducted, where lift and drag coefficients were obtained for various angles of attack, and the results were analyzed in ParaView and Gnuplot. The airfoil profile with tubercles demonstrated promising performance, particularly at high angles of attack, when compared to the profile without tubercles. These preliminary results align with expectations from existing literature. In conclusion, airfoil profiles with tubercle leading edges show potential for small wind turbine applications, considering their operational conditions at low Reynolds numbers and smaller rotor diameters. By incorporating biomimetic design elements, such as tubercles, improvements in the aerodynamic performance of small wind turbines could be achieved.*

Keywords: *biomimetics, CFD, SG6043, OpenFOAM*

1. INTRODUCTION

Flow control techniques have garnered significant interest in the research community, particularly at low Reynolds number (Re) applications, such as small wind turbines (SWT), which often experience poor aerodynamic performance due to flow separation or stall on the airfoils, leading to shortened fatigue lives. In order to be affordable to individual consumers, SWTs need to be cost-effective, reliable, and require minimal maintenance. This is often related to compromising optimal performance in favor of simplified design and operation. Consequently, small wind turbines rely on torque generated by wind acting upon the blades to start rotation. One design goal is to minimize the starting wind speed. Additionally, these turbines are frequently installed at locations where power demand exists rather than where the wind resources are the most favorable. In such low or variable wind conditions, slow startup procedures result in reduced overall energy generation (Wright and Wood, 2004).

In the past few decades, aerodynamicists have found great inspiration in bio-inspired designs. The evolutionary attributes of biological species, developed over generations, play a crucial role in their survival. This practice of biologically mimicking specific features of natural species for scientific purposes has given rise to an interdisciplinary field of study known as "Biomimetics" (Rose *et al.*, 2021).

One passive flow control technique is the implementation of leading-edge (LE) protuberances, inspired by the morphology of humpback whales' pectoral flippers, as studied by marine biologists (Fish and Battle, 1995). It has been reported that airfoils equipped with leading-edge protuberances exhibit enhanced aerodynamic lift within the post-stall region, accompanied by a more gentle and delayed stall process, resulting in extended fatigue life (Johari *et al.*, 2007; Rose *et al.*, 2021; Zhao *et al.*, 2017; Hansen *et al.*, 2011). Figure 1 shows an example of humpback whale's flippers with tubercles.

Numerous investigations have focused on improving aerodynamic performance at low Reynolds numbers using this

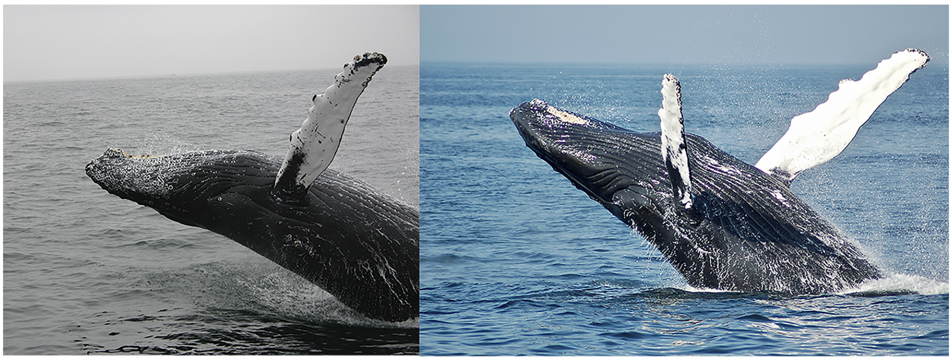

Figure 1: Humpback whale's flippers with tubercles

bio-inspired approach (Johari *et al.*, 2007; Hansen *et al.*, 2011; Zhao *et al.*, 2017; Kunya *et al.*, 2019; Miklosovic *et al.*, 2004). However, the underlying mechanisms are not yet fully understood. It is widely accepted that enhanced momentum exchange, coupled with vortex induced by the protuberances, plays a crucial role in the performance enhancement (Hansen *et al.*, 2011; Zhao *et al.*, 2017). Nonetheless, previous studies have raised doubts regarding the effectiveness of protuberances due to their larger wavelength and amplitude compared to the boundary layer thickness (Van Nierop *et al.*, 2008). To address this issue,Hansen *et al.* (2011) proposed the concept of effective protuberance height as a quantitative measure of their impact. Furthermore, Zhao *et al.* (2017) found that the ratio of effective protuberance height to boundary layer thickness should fall within the range of 0.1 to 0.5, similar to micro vortex generators. Alternative hypotheses regarding the mechanism of protuberances have also been proposed, suggesting the involvement of counter-rotating stream wise vortex and low-pressure pockets formed by leading-edge troughs (Dropkin *et al.*, 2012).

Johari *et al.* (2007) carried out an experimental study to investigate the presence of LE tubercles on a NACA 634-021 airfoil, focusing on the steady flow over the airfoils. The authors measured forces and moments within a range of angles of attack (AoA) from -6^o to 30o in a water tunnel. A combination of thee protuberances amplitudes, 0.025c, 0.05c and 0.12c (where c is the profile chord length) and two protuberances wavelengths, 0.25c and 0.50c, was implemented. Zhao *et al.* (2017) investigated the effect of LE protuberances in NACA 634-021 airfoil, for six AoA, using a wavy leading edge with an amplitude of A = 12 mm and a wavelength of λ = 25 mm. Results identified streamwise vortices as the dominant flow structure above tubercle surface within post-stall region, which was associated with the delay of flow separation.

Despite significant progress in understanding the aerodynamic performance of airfoils with protuberances, there remains a deficit of studies investigating the insertion of tubercles in SWT profiles, such as SG6043 airfoil, operating at low Reynolds numbers.

Therefore, the objective of this study is to examine the effects of protuberances on the aerodynamic performance of the SG6043 airfoil, comparing lift and drag coefficients for both geometries, with and without tubercles. The angle of attack varies from 0º to 30º, in order to capture the post-stall region. The profile SG6043 was chosen considering its relevance in SWT applications.

In the following sections we present the theory considered for the aerodynamic analysis, describe the evaluation methodology and discuss some of the obtained results. Last, we present some important concluding remarks about the numerical analyses.

2. THEORETICAL BASIS

To obtain the aerodynamic loads on the airfoil, a Navier-Stokes solver is used, by means of a Finite volume discretization. In this work, the open source software OpenFOAM is used to obtain the aerodynamic coefficients on the airfoil by means of steady flow analyses. Next, the algorithm employed is breafily explained, as well as the formulation for the aerodynamic coefficients computation.

‘

2.1 Navier-Stokes and RANS

In this study, the SIMPLE algorithm (Semi-Implicit Method for Pressure Linked Equations) is employed. It is one of the algorithms available in *OpenFOAM*. One basic equation is the momentum equation, which can be expressed in matrix form by:

$$\frac{\partial \mathbf{U}}{\partial t} + \nabla \cdot (\mathbf{U}\mathbf{U}) = \frac{-1}{\rho}\nabla p + \mu \nabla^2 \mathbf{U} + g \qquad (1)$$

where $\mathbf{U}$ is the velocity field, p is the pressure and g the body force.

By solving the momentum equation above it is possible to obtain the velocity components. For a valid solution, these components must satisfy the continuity equation, expressed as

$$\nabla \cdot \mathbf{U} = 0 \tag{2}$$

As highlighted by Jones *et al.* (2016), to form the Reynolds-Averaged equations, the variables $\mathbf{U}$ and p are written as the sum of a mean and a fluctuating part:

$$\mathbf{U} = \langle \mathbf{U} \rangle + \mathbf{U}', \; p = \langle p \rangle + p' \tag{3}$$

Averaging the above equations over an ensemble of systems then produces the RANS equations in the form:

$$\frac{\partial \langle \mathbf{U} \rangle}{\partial t} + \langle \mathbf{U} \rangle \cdot \nabla \langle \mathbf{U} \rangle = -\frac{1}{\rho} \nabla \langle p \rangle + \mu \nabla^2 \langle \mathbf{U} \rangle + \mathbf{g} - \nabla \cdot (\rho \langle \mathbf{U}'\mathbf{U}' \rangle) \tag{4}$$

where $\tau = -p\langle \mathbf{U}'\mathbf{U}' \rangle$ is the Reynolds stress tensor. To close this system of equations, τ needs to be expressed in terms of the mean variables. One way of doing this is to assume that the deviatoric part of the Reynolds stress tensor is proportional to the rate of strain tensor of the mean flow and to write:

$$-\rho \langle \mathbf{U}'\mathbf{U}' \rangle + \frac{2}{3} \rho k \mathbf{I} = 2 \rho \mu_T \langle \mathbf{S} \rangle \tag{5}$$

where $\mathbf{U}'\mathbf{U}'$ represents the deviatoric part of the Reynolds stress tensor, ρ is the fluid density, k is the turbulent kinetic energy $\mathbf{I}$ is the identity tensor μ_T is the turbulent viscosity $\langle \mathbf{S} \rangle$ is the rate of strain tensor of the mean flow.

The rate of strain tensor $\langle \mathbf{S} \rangle$ for the mean flow and the equation for turbulent kinetic energy k can be defined as follows:

$$\langle \mathbf{S} \rangle = \nabla \langle \mathbf{U} \rangle + (\nabla \langle \mathbf{U} \rangle)^T \tag{6}$$

$$k = \frac{1}{2} \langle \mathbf{U}' \cdot \mathbf{U}' \rangle \tag{7}$$

The RANS momentum equation then takes the form:

$$\frac{\partial \langle \mathbf{U} \rangle}{\partial t} + \nabla \cdot \big(\langle \mathbf{U} \rangle \langle \mathbf{U} \rangle \big) = -\frac{1}{\rho} \nabla (\langle p \rangle + \frac{2}{3} \rho k) + \mu_{\text{eff}} \nabla^2 \langle \mathbf{U} \rangle + \mathbf{g} \tag{8}$$

where $\mu_{\text{eff}} = \mu + \mu_T$. The expression for μ_T depends on the particular type of turbulence model being used. OpenFOAM employs a cell-centered finite volume approach for solving the partial differential equations governing continuum mechanics and fluid dynamics.

2.2 The SimpleFOAM

The Finite Volume discretization is considered to solve the Navier-Stokes (NS) equations, and thus Eq. (8) can be transformed into a linear system, so that

$$\mathbf{AU} = -\nabla p \tag{9}$$

where matrix $\mathbf{A}$ is a influence coefficients matrix. Here, this matrix is obtained by a Finite Volume Method discretization.

Initially, Eq. (9) is solved using the pressure field given by the initial conditions. This stage is referred to as the *Momentum* Predictor, which enables the obtaining of velocity components. However, these values usually do not satisfy Eq. (2).

Given that the coefficients of matrix $\mathbf{A}$ are known, it is possible to obtain the diagonal matrix $\mathbf{D}$, which represents the entries of the main diagonal of $\mathbf{A}$:

$$\mathbf{D} = \text{diag}(\mathbf{A}) \tag{10}$$

This way, matrix $\mathbf{D}$ is easily inverted. By manipulating the equations, it is possible to isolate an auxiliary matrix $\mathbf{H}$, which is obtained by subtracting the diagonal matrix $\mathbf{D}$ from $\mathbf{A}$:

$$\mathbf{H} = \mathbf{DU} - \mathbf{AU} \tag{11}$$

Now, $\mathbf{H}$ can be inserted into Eq. (9), so that

$$\mathbf{DU} - \mathbf{H} = -\nabla p \tag{12}$$

After some manipulation, and taking into consideration Eq. (2), the following expression can be defined:

$$\nabla \cdot (-\mathbf{D}^{-1})\nabla p = \nabla \cdot (\mathbf{D}^{-1}\mathbf{H}) \tag{13}$$

and the pressure can be obtained by the linear system solution, and inversion of $\mathbf{A}$ is avoided.

The obtained pressure field is used to update the velocity field, so that the continuity equation is satisfied. After that, $\mathbf{H}$ and p are also updated. For more information on SIMPLE, see Greenshields (2022) and **?**. The turbulence model employed was the Spalart-Allmaras model, which is a one-equation eddy viscosity model and has been widely adopted due to its simplicity and computational efficiency. For further information, see see Greenshields (2022) and **?**. This model solves a transport equation for a turbulence eddy viscosity, denoted as ν_t, which is related to the turbulent stresses in the flow and helps capture the effects of turbulence.

The transport equation for ν_t in the Spalart-Allmaras model is given by

$$\frac{D}{Dt}\left(\rho\tilde{\nu}\right) = \nabla \cdot \left(\rho D_{\tilde{\nu}}\tilde{\nu}\right) + \frac{C_{b2}}{\sigma_{\nu_t}}\rho\left|\nabla\tilde{\nu}\right|^2 + C_{b1}\rho\tilde{S}\tilde{\nu}\left(1 - f_{t2}\right) - \left(C_{w1}f_w - \frac{C_{b1}}{\kappa^2}f_{t2}\right)\rho\frac{\tilde{\nu}^2}{\tilde{d}^2} + S_{\tilde{\nu}} \tag{14}$$

where $\mathbf{U}$ is the velocity vector, t is time, ν is the molecular kinematic viscosity of the fluid, S is the magnitude of the mean strain rate tensor, given by $S = \sqrt{2\mathbf{S}\cdot\mathbf{S}}$, where $\mathbf{S}$ is the mean strain rate tensor, ϵ is the turbulent dissipation rate, f_w is a blending function that smoothly transitions between the viscous sublayer and the log-law region and c_{b1}, c_{w1}, c_{b2}, and σ are model constants.

The first term on the right-hand side represents production of turbulence due to mean strain rate, while the second term represents destruction of turbulence due to the wall, or viscous effects, the third term represents diffusion of turbulence, and the fourth term represents pressure-strain correlation effects. The Spalart-Allmaras model has been successfully adopted in a wide range of applications and is particularly suitable for aerodynamic flows, such as those encountered in this work.

2.3 Aerodynamic forces and coefficients

The blades are the wind turbine components that transform the wind energy into mechanical torque, by means of its aerodynamic shape. The blade cross section is formed by aerodynamic profiles, designed to generate forces that result in torque on the main shaft. To evaluate the efficiency of different profiles, the force coefficients curves as function of the angle of attack (AoA) are considered Hansen (2016).

The lift coefficient, C_l, and drag coefficient, C_d, can be calculated as

$$C_l = \frac{l}{\frac{1}{2}\rho U_0^2 c}, \qquad C_d = \frac{d}{\frac{1}{2}\rho U_0^2 c} \tag{15}$$

where l is the lift by unit span length, d is the drag by unit span length, U_0 is the free flow velocity, , ρ is fluid density, and c is the reference length, in this case, the profile chord.

One feature that must be addressed on the $C_l \times \alpha$ curve is the stall behavior. Despite all real fluids exhibit the effects of viscosity, transporting mass, momentum, and energy, when the influence of transport phenomena is small, the fluid can be considered inviscid and still adequately represent the flow, as flow over an airfoil. The influence of shear is limited to a small region near the airfoil surface, which characterizes the boundary layer (Anderson, 2011) However, at high AoA, the drag is large and shear has a significant influence on the flow, resulting in stall. In this condition, the flow expands around the airfoil surface and forms a wake downstream, as a result of viscosity being considered (Anderson, 2011). Therefore, the stall is the phenomenon where a loss of lift and an increase in drag occurs, typically when the AoA exceeds a certain critical value, leading to a disruption in the smooth flow of air and a decrease in overall aerodynamic performance.

3. METHODOLOGY

In this paper, to evaluate the influence of tubercles on the aerodynamic performance of the SG6043 airfoil, we performed a preliminary numerical simulation of the steady state flow over the airfoil. A baseline smooth airfoil was compared with a modified one, featuring tubercles on the leading edge. To obtain the aerodynamic characteristics of the biomimethized airfoil, the work was divided into several tasks: the basic geometry construction, the domain definition, mesh generation, NS solution and postprocessing. From the velocity and pressure fields, the aerodynamic coefficient were computed and the resulting streamlines were compared.

These steps were performed for the two models described in this work. Each task is described below, and the domain and simulation details are given.

3.1 Geometry

To investigate the influence of the tubercles, three-dimensional models were created. The basic geometry of the airfoils are shown in Fig. 2, and wer created in a 3D CAD software. Both airfoils have a chord length (c) of 1 m and a span length

(s) of 0.75 m. The wavy leading edge is characterized by an amplitude (A) of 0.025c and a wavelength (λ) of 0.25c. Tubercles are modeled by intercalating baseline airfoil profiles and re-scaled ones, which is 1.025 times the chord length.

The 3D geometries of the baseline and modified airfoils were developed in a CAD software. The geometries were then exported as a STL file definition of the computational domain. Details about the mesh are given in the next section.

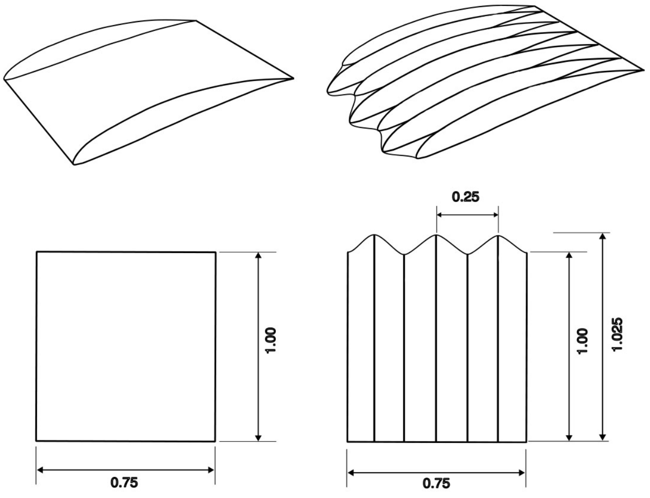

Figure 2: Basic geometry of the investigated airfoils.

3.2 Computational domain and mesh

The mesh was generated using OpenFOAM's blockMesh utility and the airfoil surface was extracted with snappyHexMesh. To generate an appropriate mesh in these tools, the domain must be divided in zones or blocks. The basic computational domain is shown in Fig. 3. The lateral sides of the domain were treated as symmetry in the spanwise direction. Field boundaries were located at $10c$ upstream, $15c$ downstream and $5c$ at top and bottom of the airfoil, which are sufficiently large for such simulation according to Zhang and Samtaney (2015); Zhang *et al.* (2015); Jones *et al.* (2008); Zhang and Samtaney (2016). As this is a preliminary study, no grid resolution investigation was conducted to confirm the results' insensitivity to mesh refinement. Further research is required to comprehensively investigate the phenomena explored in this study.

The domain was divided into six blocks, allowing finer mesh refinement in blocks B2 and B5, which are close to the airfoil surface.

To accurately capture the characteristics of the wall boundary layers, the mesh was refined near the wing surfaces using a geometric expansion technique, with addition of 10 inflation layers and the first layer height was determined as 0.001 using the snappyHexMesh utility. Figure 4 presents the mesh from three different perspectives: (a) displays the domain mesh, (b) shows the surface mesh for the baseline airfoil in perspective, and (c) presents the surface mesh for the modified airfoil from a superior view. Mesh discontinuity regions are identified in both the baseline and modified airfoil, resulting from the snappy process. However, these mesh discontinuities do not impact the lift and drag coefficients, they only affect the pressure coefficient, leading to significant noise generation.

3.3 Boundary conditions and solution

The simulation setup included a free-stream velocity (U_∞) based on a Reynolds number of 5×10^5, μ = 1.82×10^-5 and ρ = 1.225. For the simulations, the wall surfaces were set up as no-slip and adiabatic conditions.

Nine angles of attack were selected, namely 0°, 5°, 10°, 15°, 20°, 25°, 30°, 35° and 40°. The numerical results for the baseline airfoil were compared and validated with previous work (El Hady, 2020). Thereafter, lift and drag coefficients were validated with Airfoil Tools (2022) data, also for Re = 5×10^5. Finally, lift and drag coefficients were compared for the baseline profile and for the modified profile, in order to investigate the influence of tubercles on aerodynamic performance of SG6043 airfoil.

The SimpleFoam solver was employed to solve the case and convergence criteria depends on residual control for pressure and velocity, which was set sas 1×10^-5.

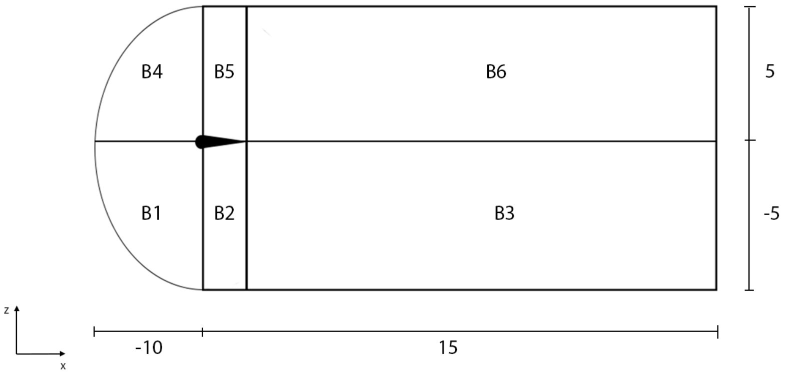

Figure 3: Dimensions of computational domain.

(a) (b) (c)

Figure 4: Mesh (a) domain, (b) Baseline airfoil and (c) Modified airfoil

4. RESULTS AND DISCUSSION

In this section we present and discuss the main results obtained for the two simulated models. In order to validate the computation, the pressure coefficient distribution numerical results are compared with those obtained by El Hady (2020). Furthermore, lift and drag coefficients are compared with AirfoilTools (2022) data.

4.1 Cp distribution

The baseline airfoil pressure coefficient, C_p, was plotted for an angle of attack of 15° and compared with the results obtained by El Hady (2020). Small discrepancies can be observed in Fig 5 (a). The airfoil with tubercles C_p shows a significant amount of noise, which may be related to discontinuities and mesh irregularities. Further study is necessary to comprehensively investigate these factors.

Evaluation of pressure distribution along the chordwise direction facilitates the identification of crucial locations that trigger adverse pressure gradients, as depicted in Fig 5 (b). When operating at higher AoA, in this case, 35 °, separation of the airflow appears to be predominantly present on the suction side of the airfoil. Nevertheless, the modified leading edge design preserves reduced pressure levels, what has been accredited by Rose *et al.* (2021) to contribute to the generation of sustained lift in the post-stall region. The existence of strong pressure gradients near the leading edge could potentially account for the delay and prolongation of the stall characteristics.

Figure 6 shows the pressure on the airfoil surfaces, where it is possible to identify a uniform pressure distribution on the LE region for the smooth airfoil, while the modified airfoil shows lower pressure regions near the roots and higher pressure regions at the tips. This preliminary finding aligns with Rose *et al.* (2021) observations, where a delayed separation of boundary layer was identified on the suction airfoil region, due to the pressure gradient between peaks and roots of the tubercles. Therefore, the fluid remains attached to the airfoil at high angles of attack, contributing to smoother stall phenomenon.

4.2 Lift and drag coefficients

Figure 7 (a) presents the curves for the lift coefficient C_l versus the angle of attack α for the smooth profile, with blue points, witch can be compared with the reference AirfoilTools (2022), in purple, both at $Re = 5 \times 10^5$. The validation is presented only for 0° to 18° angles of attack, which was the available data at AirfoilTools (2022). The maximum Cl point coincides for the baseline airfoil investigated in this work and for the reference, approaching a 15° angle of

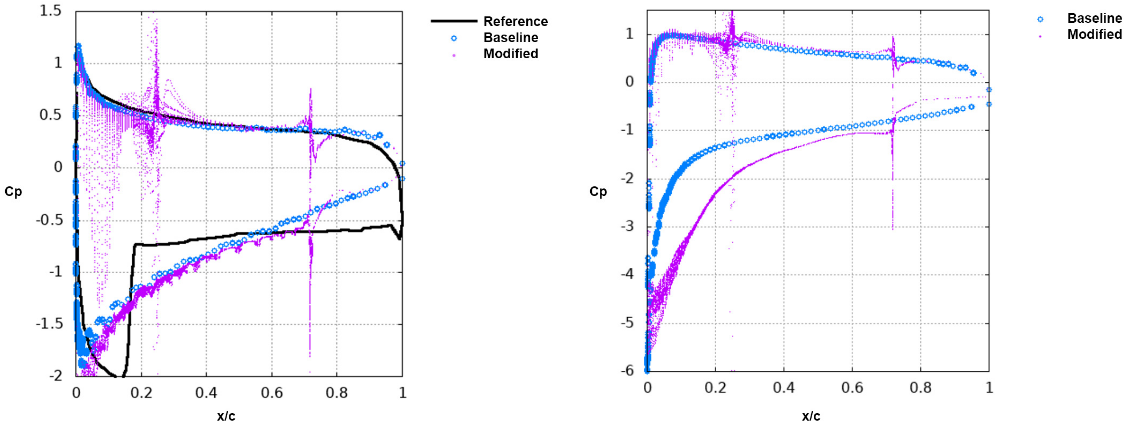

(a) (b)

Figure 5: Pressure coefficient distribution for (a) 15° and (b) 35°. Reference: El Hady (2020). Baseline and Modified: current work.

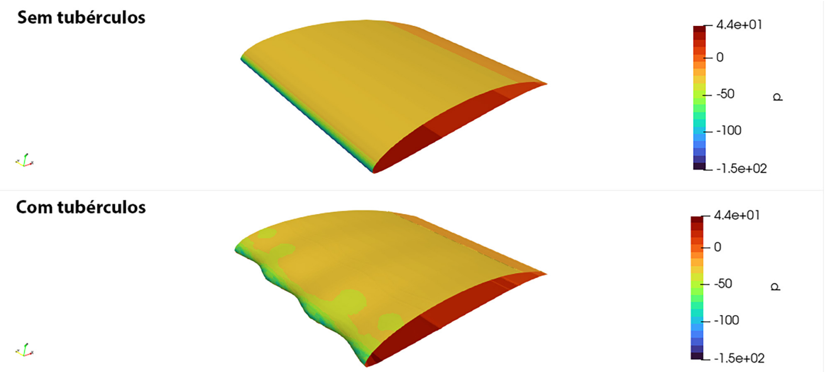

Figure 6: Pressure distribution over baseline and modified airfoils from the current work.

attack. A smother stall pattern can be identified at high AoA, where Cl reaches higher values for the tubercled airfoil. This seemingly simple result holds significant potential for application in low Reynolds number regimes employing the SG6043 airfoil profile. Further detailed investigations should address the influence of variations in tubercle wavelength and amplitude specifically for this aerodynamic profile.

Similarly, the simulation results for drag coefficient, Cd, are compared to reference data. Figure 7 (b) shows the data in orange and the smooth profile result in red. Results follow the reference pattern between 0 and 18°, although, there is a slight shift in the curve.

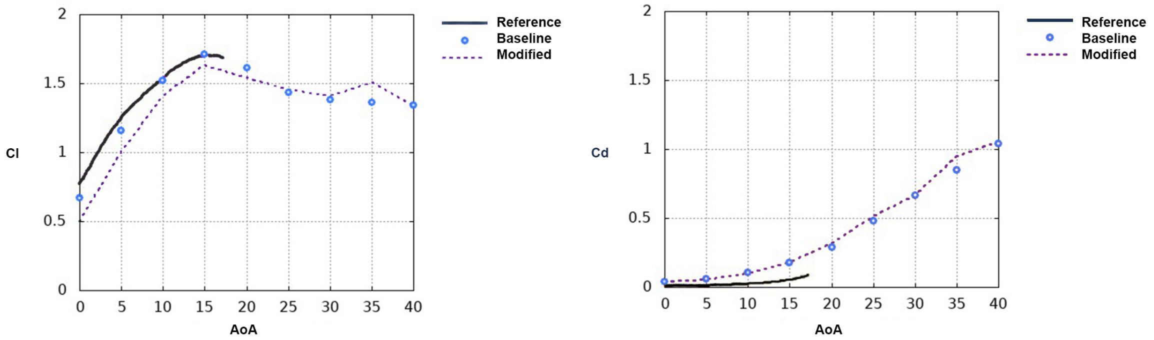

(a) (b)

Figure 7: Comparison of (a) lift coefficient and (b) drag coefficient. Reference: Airfoil Tools (2022), Baseline and Modified: current work .

The study of flow characteristics reveals potential of flow control by biomimetic tubercles and the streamline patterns play an important role. Fig. 8 shows the streamlines pattern for the baseline airfoil, at AoA of 15°and 35°. On the other hand, Fig. 9 presents streamlines for the modified airfoil, at 15°and 35°AoA. At 15°, the flow remains laminar for both profiles, but at 35°a different pattern is evident for the two airfoils. It has been reported by Hansen *et al.* (2016), the formation of a reverse flow pattern in the separation region, given that the arrangement of tubercles alters the airflow trajectory, inducing the formation of swirling vortices that roll over the suction region, keeping the flow attached to the surface. This phenomenon is associated with the smoother stall process and may be related to the streamlines pattern observed.

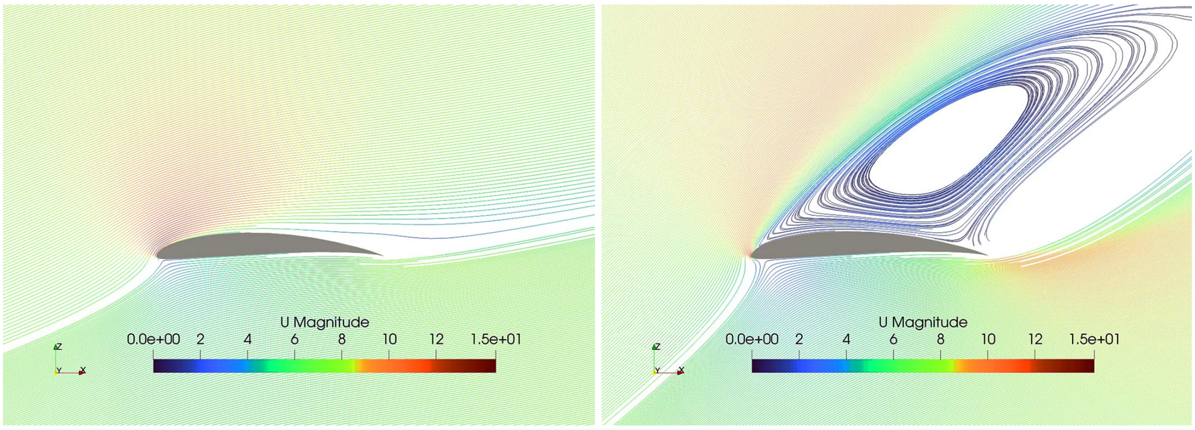

(a) (b)

Figure 8: Streamlines over smooth airfoil at AoA (a) 15°(b) 35°

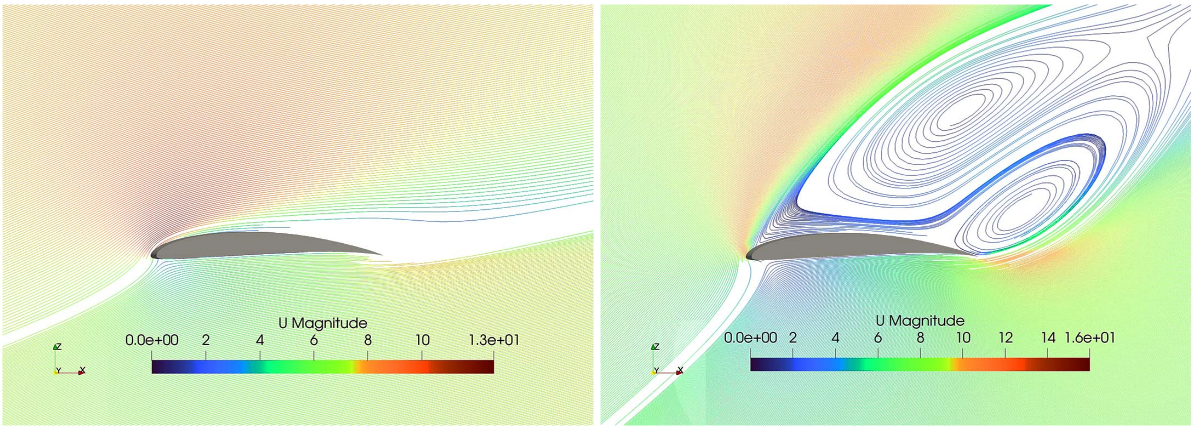

(a) (b)

Figure 9: Streamlines over tubercled airfoil at AoA (a) 15°(b) 35°

5. CONCLUDING REMARKS

The biomimetic flow control technique, inspired by Humpback Whales flippers, reveals potential for small wind turbine applications through the study of pressure distribution, aerodynamic coefficients and flow characteristics at the LE region. Overall, the initial numerical results demonstrated a reasonable agreement with the reference data. However, further research is necessary to thoroughly investigate the phenomena explored in this study, including an examination of mesh grid resolution and sensitivity to mesh refinement. For example, the presence of noise in the Cp distribution is thought to be linked to mesh discontinuities. Stall phenomenon was characterized by a sudden change in lift and drag coefficient occurring around 15°AoA for the smooth airfoil, which tends to be aligned with literature results.

Airflow characteristics around the modified airfoil can be visualized in the corresponding changes of lift and drag coefficients within the pre-stall and post-stall regions. The distributions of pressure coefficients along the x-direction at 15°and 35°angles of attack, comparing the baseline airfoil and the modified one, reveal that the aerodynamic suction around leading edge is similar for both profiles at 15°AoA, while the lift coefficient remains close to slightly lower, for the tubercled profile. However, at 35°AoA, Cp distribution reveals an increase in aerodynamic suction for the modified profile compared to the baseline, resulting in higher lift coefficients observed at this angle of attack. These qualitative analyses show potential, and further studies are underway to better understand the influence of the leading-edge tubercles on the SG6043 airfoil.

The smoother stall process which is observed for the profile with tubercles, at high angles of attack, 25°to 40°, has potential to improve fatigue life of small wind turbines, which is beneficial once their blades rotate at higher speeds compared to large-scale turbines. Furthermore, the higher lift values at the port-stall region can contribute to turbine activation, as the absence of blade pitch control in small HAWTs relies on lift generated at high angles of attack to overcome the torque of the drivetrain and generator. This would enable small wind turbine installation at low wind speeds locations, contributing to the expansion of renewable electricity sources.

6. REFERENCES

Airfoil Tools, 2022. “Airfoiltools: Sg6043”. SG6043 (sg6043-il) SG6043 - Selig / Giguere SG6043 wind turbine airfoil (high L/D), http://airfoiltools.com/airfoil/details?airfoil=sg6043-il. Accessed 26 November 2022.

Anderson, J.D.J., 2011. *Fundamentals of Aerodynamics*. Mc Graw Hill, New York.

Dropkin, A., Custodio, D., Henoch, C.W. and Johari, H., 2012. “Computation of flow field around an airfoil with leading-edge protuberances”. *Journal of Aircraft*, Vol. 49, pp. 1345–1355.

El Hady, M.A., 2020. “A comparative study for different shapes of airfoils”. *Journal of Advanced Research in Fluid Mechanics and Thermal Sciences*, Vol. 69, pp. 34–45.

Fish, F.E. and Battle, J.M., 1995. “Hydrodynamic designof the humpback whale flipper”. *Journal of Morphology*, Vol. 225, pp. 51 – 60.

Greenshields, C., 2022. *OpenFOAM v10 User Guide*. The OpenFOAM Foundation, London, UK.

Hansen, K.L., Kelso, R.M. and Dally, B.B., 2011. “Performance variations of leading-edge tubercles for distinct airfoil profiles”. *AIAA Journal*, Vol. 49, pp. 185–194.

Hansen, K.L., Rostamzadeh, N., Kelso, R.M. and Dally, B.B., 2016. “Evolution of the streamwise vortices generated between leading edge tubercles”. *Journal of Fluid Mechanics*, Vol. 788, pp. 730–766.

Hansen, M.O.L., 2016. *Aerodynamics of Wind Turbines*. Earthscan, London.

Johari, H., Henoch, C., Custodio, D. and Levshin, A., 2007. “Effects of leading-edge protuberances on airfoil performance”. *AIAA Journal*, Vol. 45, pp. 2634–2642.

Jones, D.A., Chapuis, M., Liefvendahl, M., Norrison, D. and Widjaja, R., 2016. “Rans simulations using openfoam software”. *Defence Science and Technology Group: Fishermans Bend, VIC, Australia*.

Jones, L.E., Sandberg, R.D. and Sandham, N.D., 2008. “Direct numerical simulations of forced and unforced separation bubbles on an airfoil at incidence”. *Journal of Fluid Mechanics*, Vol. 602, pp. 175–207.

Kunya, B.I., Folayan, C.O., Pam, G.Y., Anafi, F.O. and Muhammad, N.M., 2019. “Performance study of whale-inspired wind turbine blade at low wind speed using numerical method”. *CFD Letters*, Vol. 11, pp. 11–25.

Miklosovic, D.S., Murray, M.M., Howle, L.E. and Fish, F.E., 2004. “Leading-edge tubercles delay stall on humpback whale (megaptera novaeangliae) flippers”. *Physics of fluids*, Vol. 16, pp. 39–42.

Rose, J.B.R., Natarajan, S.G. and Gopinathan, V.T., 2021. “Biomimetic flow control techniques for aerospace applications: A comprehensive review”. *Reviews in Environmental Science and Bio/Technology*, Vol. 20, pp. 645–677.

Van Nierop, E.A., Alben, S. and Brenner, M.P., 2008. “How bumps on whale flippers delay stall: An aerodynamic model”. *Physical Review Letters*, Vol. 100, p. 054502.

Wright, A.K. and Wood, D.H., 2004. “The starting and low wind speed behaviour of a small horizontal axis wind turbine”. *Journal of Wind Engineering and Industrial Aerodynamics*, Vol. 92, pp. 1265–1279.

Zhang, W., Cheng, W., Gao, W., Qamar, A. and Samtaney, R., 2015. “Geometrical effects on the airfoil flow separation and transition”. *Computers & Fluids*, Vol. 116, pp. 60–73.

Zhang, W. and Samtaney, R., 2015. “A direct numerical simulation investigation of the synthetic jet frequency effects on separation control of low-re flow past an airfoil”. *Physics of Fluids*, Vol. 27.

Zhang, W. and Samtaney, R., 2016. “Assessment of spanwise domain size effect on the transitional flow past an airfoil”. *Computers & Fluids*, Vol. 124, pp. 39–53.

Zhao, M., Zhang, M. and Xu, J., 2017. “Numerical simulation of flow characteristics behind the aerodynamic performances on an airfoil with leading edge protuberances”. *Engineering Applications of Computational Fluid Mechanics*, Vol. 11, pp. 193–209.

7. RESPONSIBILITY NOTICE

The author(s) is (are) solely responsible for the printed material included in this paper.